LSPR-based colorimetric immunosensor for rapid and sensitive 17β-estradiol detection in tap water

Antonio Minopoli[a,b], Nikola Sakač[c], Bohdan Lenyk[b,d], Raffaele Campanile[a], Dirk Mayer[b], Andreas Offenhäusser[b], Raffaele Velotta[a], Bartolomeo Della Ventura[a,e,*]

[a]Department of Physics "E. Pancini" – Università di Napoli Federico II – Via Cintia, 26 Ed. 6 – 80126 Napoli, Italy

[b]Institute of Complex Systems (ICS-8), Bioelectronics, Forschungszentrum Jülich, 52428 Jülich, Germany

[c]Faculty of Geotechnical Engineering, University of Zagreb, Hallerova 7, 42000 Varaždin, Croatia

[d]Department of Physics, University of Konstanz, 78457 Konstanz, Germany

[e]Department of Physics, Politecnico di Milano, Piazza Leonardo da Vinci 32, 20133 – Milano, Italy

ABSTRACT

We propose a highly sensitive immunosensor based on the Localized Surface Plasmon Resonance (LSPR) for 17β-estradiol (E2) quantification in water. E2 molecules are recognized by polyclonal antibodies immobilized onto gold nanoparticles (AuNPs) and act as linkers that cause nanoparticles aggregation. This leads to the change in the optical properties of the solution visible even by naked eyes. The aggregates were characterized by Dynamic Light Scattering (DLS) and Scanning Transmission Electron Microscopy (STEM) and provided an accurate assessment of the inter-particle distance. The finite-difference time-domain (FDTD) method applied to a Mie problem like workspace allowed us to describe the optical behaviour of the AuNP aggregates with excellent agreement between the experimental and numerical results. The limit of detection (LOD), without any preconcentration step, is 3 pg/mL (11 pM), whereas the detection range extends over five decades up to 10^5 pg/mL. The proposed E2 immunosensor was tested in tap water, where no significant cross-reaction signal was detected by similar molecules (testosterone, progesterone, estrone and estriol). The device described here represents a significant improvement of low E2 levels determination in terms of affordability, time and measuring simplicity, making it suitable for environmental applications.

Keywords:

Gold nanoparticles; localized-surface plasmon resonance; colorimetric immunosensor; 17β-estradiol; photochemical immobilization technique; antibodies.

1. Introduction

17β-estradiol (E2) is an estrogen naturally secreted by the ovaries and involved in several hormonal [1] and carcinogenesis processes in human [2]. Its detection in blood and urine in small concentration is very attractive in medical diagnostics to address menopause symptoms, ovaries and breast cancer, gynecomastia and in pregnancy or infertility treatments. Although many researches in the field of medicine and toxicology deal with estrogens, there is a lack of information about their presence in the environment [3,4], a serious issue given their abundant use in dairy livestock industry to enhance cattle growth rates, feed efficiency and to procure lean muscle mass [5]. The presence of estrogens in waste waters and agriculture lands [6,7] can lead to bioaccumulation and biomagnification in the ecosystems; for instance, E2 in low concentration from 0.1 to 1 ng/L may cause estrogen response in male fish [3]. It is worth noticing that such a concentration is lower than that usually detected in the environment [8,9], making urgent the need for developing analytical methods and sensors for continuous water monitoring and mapping of the potential contamination points.

In laboratories, estradiols are usually determined by High-Performance Liquid Chromatography (HPLC) or Liquid Chromatography – Mass Spectrometry (LC-MS) reaching LODs up 0.03 ng/L [10]. These methodologies use expensive instrumentation, require trained personnel and spend significant amounts of toxic solvents. A partial alternative is provided by immuno-techniques, like Enzyme-Linked ImmunoSorbent Assay (ELISA), currently the main technique for routine E2 detection in real samples (serum or urine). Most of the available ELISA assays provide a large detection range from 10 to 1000 pg/mL [11], but the technique is limited by the assay time (up to 3 hours), the relatively high cost of the kits and a need for a skilled personnel. Thus, reliable, fast and easy-to-use biosensors are highly desirable as tools for E2 detection at low concentrations in water.

One possible approach relies upon the recognition of estradiol molecules by using electrochemical [12–14], optical [15–19] or chromatographic [20] techniques. Even though they can reach LODs in the fM

range [12] (see table 1), their current complexity in terms of time-consumption, expensive materials and complex realization [12], as well as the occurrence of interference from other analytes commonly present in natural waters, still represent an issue to overcome [21]. In this regard, colorimetric biosensors based on colloidal solution of gold nanoparticles (AuNPs) are very attractive since they provide a fast and accurate response with a very high sensitivity and easiness-of-use.

Metal nanostructures, such as AuNPs, exhibit unique plasmonic properties due to their capability to confine the electromagnetic (EM) waves within the near-field region close to the surface [22]. This provides them with unique features; such as extremely large electric field enhancements [23], nano-antenna [24], huge light scattering and absorption [25], and striking photothermal conversion capabilities [26]. In the last years, considerable efforts have been performed in order to exploit plasmonic properties of the nanostructures in the biosensor field. Several different plasmonic biosensors were developed to improve the sensitivity and to reduce the response-time [17,27,28]. One of the most attractive are AuNPs-based colorimetric biosensors since they are cheap, simple to manufacture and extremely sensitive. The absorbance wavelengths of noble metal nanospheres (gold and silver) are in the visible region thereby giving rise to the vivid colors of their colloidal solutions [29,30]. The color depends both on their diameter [29] and on the surrounding medium [30]. Gold is generally preferred to silver because of its biocompatibility [31], inertness [32] and surface chemistry [33].

As it concerns bioreceptors, antibodies (Abs) offer high specificity in the antigen detection and simplicity in the gold surface functionalization [34]. In fact, it was demonstrated that Abs immobilization on the gold surface with upright orientation can be easily achieved by activating them with a UV light before the functionalization [35–37]. This procedure, named Photochemical Immobilization Technique (PIT), improves considerably the sensitivity of the biosensor because it leads to oriented antibodies with their fragment antigen-binding site (Fab) exposed to the solvent. The effectiveness of the PIT was already confirmed in several biosensing applications [38–41].

In this paper, we propose a picomolar colorimetric immunosensor for E2 in tap water, without any sample preconcentration step. The immunosensor consists of a colloidal solution of functionalized AuNPs (Ab-AuNPs) that aggregate in presence of E2 (figure 1) within few minutes after the analyte is added and the solution is stirred. The clustering gives rise to a colour change, from red to purple, due to the red-shift of the absorption peak. The AuNP clusters were characterized by Dynamic Light Scattering (DLS) and

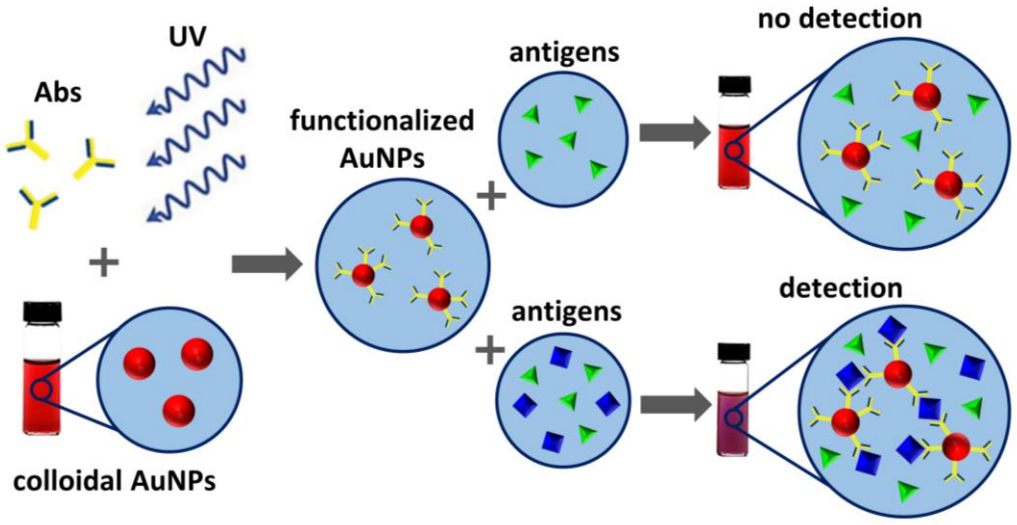

Fig. 1. Detection scheme of a colorimetric immunosensor based on a colloidal solution of functionalized AuNPs with antibodies. The analytes act like linkers due to multiple binding sites allowing the AuNP aggregation.

Scanning Transmission Electron Microscopy (STEM). The latter technique highlighted the presence of the Ab layer surrounding the nanoparticles through the measurement of the inter-particle distance in AuNP clusters. The measured distance was approximately 10 nm and this allowed us to simulate the optical response of the AuNP clusters as a function of their size, which in turn depends on the E2 concentration. The high performance, both in term of LOD and detection range, makes this colorimetric immunosensor very attractive compared other biosensors (table 1).

Table 1
Comparison among biosensors for the E2 detection

Transducer	Bioreceptor	Method	LOD	Detection range	Reference
Rhodamine B fluorescence quenched by AuNPs	aptamers	fluorescence	0.48 nM	0.48-200 nM	[15]
FRET-based turn-on fluorescence	aptamers	fluorescence	0.35 nM	0.35-35000 nM	[16]
Colloidal solution of AuNPs	aptamers	colorimetry	0.367 nM	0.367-367000 nM	[17]
TiO2-BiVO4 heterostructure	aptamers	photoelectrochemistry	22 fM	0.1-250 pM	[12]
Electrochemical sensor using split aptamers	aptamers	electrochemistry	0.5 pM	1.5-7000 pM	[13]
Nanostructured magnetic molecularly imprinted polymers	MIP	electrochemistry	20 nM	$50\text{-}10^4$ nM	[14]
Indirect probe based immunochromatography assay	antibody	chromatography	0.7 nM	0.7-18 nM	[20]
Carboxymethylated dextran-coated gold sensor chip	antibody	SPR	7 nM	0.5-20 nM	[18]
11-MUA/E2-BSA conjugate on gold sensor chip	antibody	SPR	3.6 pM	$36\text{-}3.6\cdot10^6$ pM	[19]
Colloidal solution of AuNPs	antibody	colorimetry	11 pM	$11\text{-}10^5$ pM	Present study

2. Materials and methods

2.1. Materials

Gold(III) chloride hydrate ($HAuCl_4 \cdot H_20$), sodium citrate dihydrate ($C_6H_5Na_3O_7 \cdot 2H_2O$), bovine serum albumin (BSA) and 17β-estradiol ($C_{18}H_{24}O_2$) were purchased from Sigma-Aldrich while polyclonal sheep anti-17β-estradiol IgG antibodies (anti-E2) from RayBiotech. The buffer for all the preparations was ultrapure water dispensed by a Milli-Q® system.

2.2. AuNP synthesis and centrifugation

The AuNPs were synthesized via chemical reduction of chloroauric acid ($HAuCl_4 \cdot H_2O$) by means of sodium citrate ($Na_3C_6H_5O_7$) according to Pollitt's protocol [42]. A solution composed of 0.5 mL solvated $HAuCl_4 \cdot H_2O$ (24 mM) and 50 mL of ultrapure water was warmed at 150 °C with vigorous constant stirring. During the boiling, 6 mL of sodium citrate dihydrate (39 mM) was added into the solution to

achieve particle nucleation. After 2 minutes, another 4.2 mL of $HAuCl_4 \cdot H_2O$ (24 mM) was added to induce particle growth. Within some minutes, the solution colour moved from transparent to black and finally to bright red. The solution was let cool down for 2 hours keeping the same stirring. The colloidal solution was firstly characterized by the UV-vis spectrophotometer to assess the AuNP quality. 200 µL of the solution diluted into 800 µL of ultrapure water provides a Localized Surface Plasmon Resonance (LSPR) wavelength of 529 nm and an optical density (OD) of 1.4-1.5. It was possible to store the solution in the fridge (4 °C) for longer time. In order to use the AuNPs like a colorimetric biosensor, it was necessary to remove as much sodium citrate as possible to avoid AuNP aggregation during the Ab functionalization. We optimized the centrifuge protocol by tuning the number of centrifugations, the acceleration and the duration. This was done in order to balance the amount of AuNPs that precipitated and aggregated irreversibly, and the efficiency to remove the supernatant leaving the re-suspendable pellet. The best centrifuge protocol working conditions for 1 mL of citrate AuNPs (the dilution: 200 µL of citrate AuNPs and 800 µL of ultrapure water) was achieved through two centrifuge steps: a) 15 min at 9000 g, and b) 10 min at 5000 g. After each centrifugation, the pellet was re-suspended in 1 mL ultrapure water. This resulted in OD reduction to ~1.0 that corresponds to ~10^{11} AuNPs/mL with diameter of 35 nm [43].

2.3. Ab functionalization by PIT

The AuNP functionalization was achieved by PIT [35–37]. A volume of 1 mL of anti-E2 (18 µg/mL) was irradiated by an UV-lamp for 30 s. The UV reactor consisted of two low pressure mercury lamps each providing 2 W at 254 nm. The lamps were of 10 mm diameter tube mounted in a stacked U-shape configuration so that a standard 10 mm cuvette could be housed inside the internal volume (Pro Com Alta Tenologia S.r.l.). Given the proximity of the cuvette to the lamps and the wrapping geometry, we estimated that the solution was exposed to an UV irradiation whose intensity was 1 W/cm^2. A volume of 25 µL of irradiated Ab solution was added to 1 mL of AuNPs (in ultrapure water) with an OD ~1.0 (the corresponding anti-E2 concentration in the final solution was 450 ng/mL, namely ~2×10^{12} Abs/mL). Such a volume

was added in 5 spikes (5 μL each one) followed by gentle stirring to avoid AuNP aggregation. This procedure was a result of an empirical study on the functionalization (figure S1). In this regard, different amounts of anti-E2 were tested to assess the behaviour of the LSPR shift. We observed that the absorption peaks red-shifted as the anti-E2 concentration increased until 1 μg/mL, that corresponded to a maximum red-shift of 5 nm. For greater amounts of anti-E2, no change in LSPR wavelengths were observed due to the saturation. We chose to halve the anti-E2 concentration that corresponded to the AuNP saturation both for reducing the amount of unbound Abs into the solution and for keeping low the number of Abs onto the AuNPs to assure the conditions that guarantee an optimal response of the device [44]. Therefore, assuming that most of Abs bounded to the gold surface, the average number of Abs onto the AuNPs was ~20 Abs/AuNP. The absorbance spectra of the functionalized AuNPs showed a red-shift of the LSPR of about 3 nm. Finally, 1 mg/mL of bovine serum albumin (BSA) was added in order to block the AuNP surface from nonspecific adsorption. The further 2 nm of red-shift entailed to the BSA was consistent with AuNPs unsaturated by Abs.

2.4. Colorimetric immunoassay

The different concentrations of E2 in tap water were achieved by serial dilutions starting from a stock concentration of 20 μg/mL. A small volume of 20 μL of each sample was added in one spike into 1 mL of Ab-AuNPs (OD ~ 1.0) to achieve a local high concentration of E2 while leaving essentially unchanged the total volume, and, hence, the Ab-AuNP concentration. Although mechanical pipetting would speed up the system kinetics by reducing the detection time down to few minutes, we chose to gently shake the solution by vortex mixer (10 s) in order to ensure the reliability and reproducibility of the results without any operator dependence. Such a short mixing time increased the binding effectiveness between E2 molecules and the Ab-AuNPs, while leaving the latter at rest. After mixing, the solution was left to reach the equilibrium via diffusion of complexed AuNPs (E2-Ab-AuNPs) into the whole reaction volume (1 mL) for 3 hours, a time long enough to warrant the reach of the equilibrium [45]. The difference between the

absorption peak after and before the E2 detection provided the LSPR shift, which was correlated to the E2 concentration.

2.5. Repeatability, stability, recovery and specificity assay

The repeatability of the colorimetric immunosensor response was evaluated by performing different measurements at E2 concentration of 10 pg/mL with ten samples of 1 mL citrate AuNPs, picked up from the same starting stock solution, then centrifuged and functionalized separately. The stability was studied through the absorption spectra of a single sample at E2 concentration of 10 pg/mL at different time intervals after the first measurements. The recovery was measured as the ratio between the theoretical E2 concentration provided by the dose-response curve and the corresponding nominal value. The specificity was tested on the most competitive molecules of 17β-E2 like progesterone, estrogens (E1 and E3) and testosterone. Two different concentrations of each analyte were tested: 10 pg/mL (optimal for E2 detection) and 100 ng/mL (an exceeding concentration) in order to assess the absence of nonspecific detection even in presence of very high interfering analyte concentration.

2.6. Instruments

Sample characterization was performed via UV-vis spectroscopy, DLS and STEM. The UV-vis absorption spectra were recorded on an UV/vis spectrophotometer (model 6715 Jenway, Cole-Parmer® Company) with 0.1 nm resolution and 0.2 nm spectral bandwidth. The DLS measurements were carried by a particle size analyser (model Zetasizer Nano ZS, Malvern Instruments Company) equipped with a 633 nm He−Ne laser and an avalanche photodiode detector placed at the detection angle of 173°. The STEM images were acquired by an electron microscope (model FEI Magellan 400 XHR SEM, Nanolab Technologies Company) equipped by ELSTAR® monochromatic e-beam column able to achieve a resolution of 0.8 nm at 25.00 kV at the optimum working distance (WD). The images were recorded by detecting the transmitted electrons. Before the STEM measurements, each sample was diluted 1:1000 to prevent false-positive clusters due to the approaching or overlapping of AuNPs during the drop drying on the TEM

grid. Furthermore, only the middle cells of the grids were acquired in order to avoid any artefacts at the edge due to the coffee ring effects.

3. Results and discussion

3.1. Dose-response curve

The AuNPs were synthesized by chemical reduction of chloroauric acid with the use of sodium citrate according to Pollitt's protocol [42]. The AuNP characterization was performed by UV-vis absorption spectroscopy, DLS and STEM (figure S2). The LSPR wavelengths are 528.5 nm for naked AuNPs, as expected for a gold nanosphere with a diameter of 35 nm [29,43], and 531.4 nm for Ab-AuNPs. The functionalization gave rise to a dielectric shell surrounding nanoparticles that yielded a red-shift of the LSPR of about 3 nm. The DLS measurements confirmed the AuNP size, providing a hydrodynamic diameter of about 36.6 nm for the naked AuNPs and 45.3 nm for the functionalized. A quantitative analysis of the STEM images corroborates the previous results providing an average diameter of about 32 nm (figure S3).

Since the tap water contains salts that would induce non-specific nanoparticle aggregation, it was important to keep as low as possible the volume of the sample to be analysed. A volume of 20 μL tap water diluted in 1 mL of ultrapure water with Ab-AuNPs, provided a good compromise between a negligible red-shift of the absorption peak and a large volume that would allow large sensitivity and small error. Figure 2b shows the absorption spectra of samples of E2 at different concentrations (absorption spectra at all the concentrations are shown in the figure S4a). The LSPR peak exhibits a measurable red-shift for concentrations higher than ~3 pg/mL with a marked effect in the range 8-12 pg/mL. Higher concentrations prevented the complexed AuNPs from forming larger clusters, and hence the red-shift was reduced (*hook effect* [46]). This behaviour was visible even by naked eyes, as figure 2a shows: The colour of the solution moved from pink to purple as [E2] reached 10 pg/mL returning to pink as the concentration was further increased. The possibility to get a qualitative *in situ* response, seen even by naked eyes without any specialized instrumentation, makes the proposed immunosensor practical and easy to use.

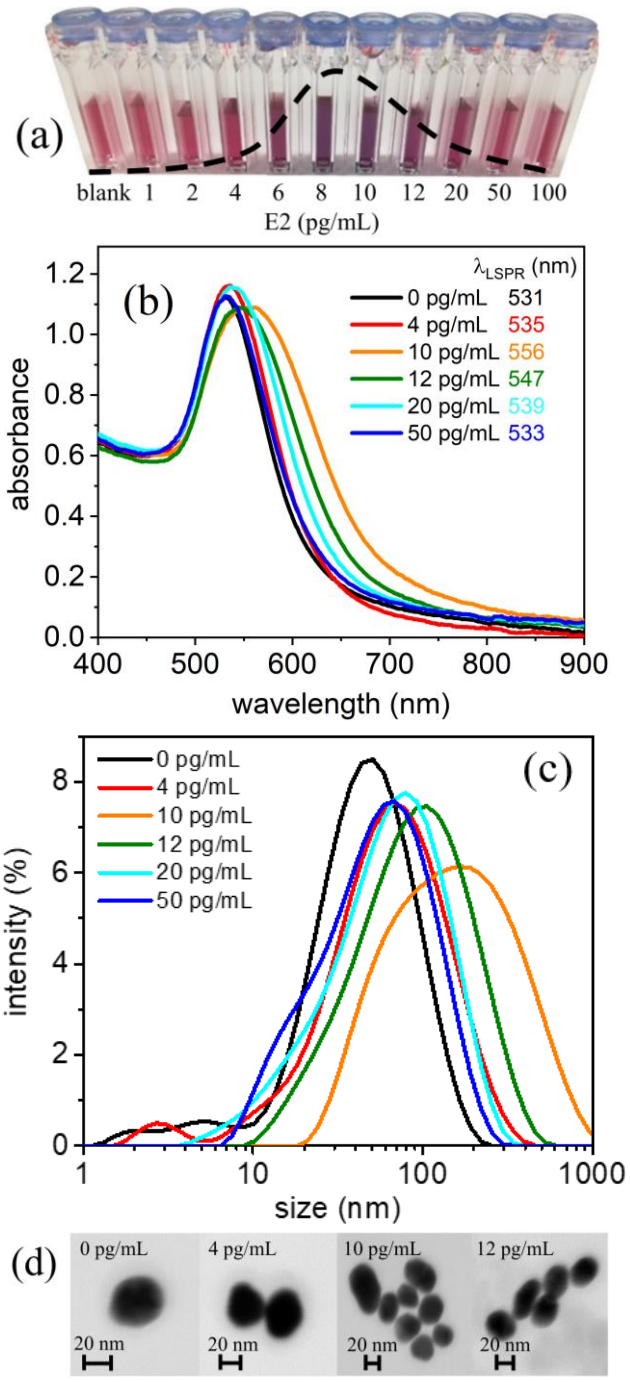

Fig. 2. (a) Color change induced by AuNP aggregation. The dashed black line showed qualitatively the behavior of the colorimetric test in its detection range. The maximum color change towards purple was achieved around 8-10 pg/mL. (b) Absorption spectra, (c) DLS measurements and (d) STEM images at high magnification acquired at different E2 concentration in tap water. The absorption peak red-shifts until a concentration of 10 pg/mL beyond which it blue-shifts due to the saturation of Ab binding sites. Similarly, the hydrodynamic diameter of the clusters increased up to 162.4 nm corresponding to 10 pg/mL of E2 and then it decreased for higher concentration.

The aggregation dynamics was quantitatively evaluated via DLS (figures 2c and S4b) and STEM (figures 2d and S5). Both techniques confirm that the behaviour of the absorption spectra as a function of the E2 concentration is due to the aggregation of complexed AuNPs. The hydrodynamic diameter increased from 48.5 nm ([E2] = 0 pg/mL) to a maximum of 162.4 nm ([E2] = 10 pg/mL), to reduce to 66.3 nm for larger E2 concentration. Similarly, the STEM images (figure S5) of the colloidal solution showed (i) only single nanoparticles for the control ([E2] = 0 pg/mL), (ii) large aggregates for E2 concentrations in the range 8-12 pg/mL and (iii) dimers and trimers at higher E2 concentrations (>20 pg/mL).

The spectra in the figure 2b were fitted by a Gaussian curve around the absorption peak and the LSPR shifts are reported in the figure 3 as a function of the E2 concentration in tap water. The concentration that provided the largest red-shift is the so-called *hook point*, and corresponds to the optimal concentration that ensures the dynamic equilibrium between the largest aggregates of AuNPs and the cluster instability due to electrostatic repulsion and steric hindrance [30]. For E2 concentrations lower than ~10 pg/mL the analyte was insufficient to yield large AuNP clusters and the LSPR red-shift was only 4-6 nm, thereby

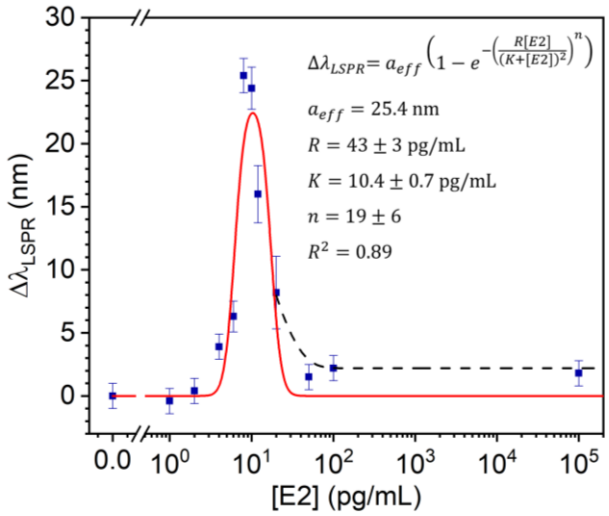

Fig. 3. Shift of the absorption peak as a function of E2 concentration in tap water (dose-response curve). The dashed line is included to guide the eye to highlight the presence of a detectable signal even at very high E2 concentration, whereas the red line is the best fit of the experimental data with the equation (6), which does not capture the asymptotic behaviour of the dose-response curve.

suggesting complexed AuNP dimerization [47] in accordance with DLS and STEM measurements (figures S4b and S5, respectively). On the other hand, an excess of E2 molecules led to the occupation of most of the Ab binding sites thereby hindering the formation of large AuNP aggregates (figure S5).

Even though in our scheme the *hook effect* arose, it is worth noticing that even at very high E2 concentrations the LSPR shift was still measurable (figure 3). We can explain such an advantageous feature by assuming that the aggregation dynamics consisted of two steps with different temporal dynamics: The first step concerned the interaction between the E2 molecules and Ab-AuNPs whereas the second took place on a longer time scale and was related to the interaction between E2-Ab-AuNPs and Ab-AuNPs. The initial gentle shaking (by vortex mixer) enhanced the probability that an Ab-AuNP bound the free E2 molecule within the region where the sample drop was released (~20 μL), such a region being much smaller than the whole volume (1 mL). In this limited region, the saturation of the Ab binding sites could well be reached, but afterwards the diffusion took place and the aggregation could occur among E2-Ab-AuNPs and the distanced Ab-AuNPs (in the whole sample volume) on a much longer time scale [45]. Therefore, even if the E2 molecules locally saturated the binding sites, the subsequent diffusion of E2-Ab-AuNPs ensured the formation of dimers or trimers with Ab-AuNPs encountered during the diffusion (figure S5).

3.2. Morphological characterization of AuNP aggregates

The average number of AuNPs that form the aggregates was evaluated from STEM images with low magnification (figure S5). The average number was approximately 12 AuNPs for the clusters corresponding to 10 pg/mL of E2. Concerning AuNPs aggregation, a quantitative analysis of STEM images with high magnification was performed in order to evaluate the inter-particle distance due to both the Abs and the analyte (figure 4a and 4b). Such a distance turned out to be approximately 10 nm and is compatible with a dielectric shell thickness of about 5 nm and a negligible size of the analyte. Finally, in order to investigate the assumption that the distance among AuNPs was actually due to the Ab-functionalization,

a quantitative analysis of salt-induced aggregates of non-functionalized AuNPs was performed (figure S6). The vanishingly small inter-particle distance in absence of Abs corroborated the assumption according to which the nanoparticles in figure 4a were AuNP surrounded by a 5 nm of Ab shell.

3.3. Optical response of AuNP aggregates (numerical simulations)

The optical response of the AuNP aggregates was simulated by the "FDTD solutions" tool of Lumerical software that solves the Maxwell's equations via the finite-difference time-domain (FDTD) method within a Mie problem-like workspace. Briefly, the workspace consisted of light source, plasmonic nanostructure, surrounding medium, photodetector and appropriate boundary conditions (BCs) and was discretized over

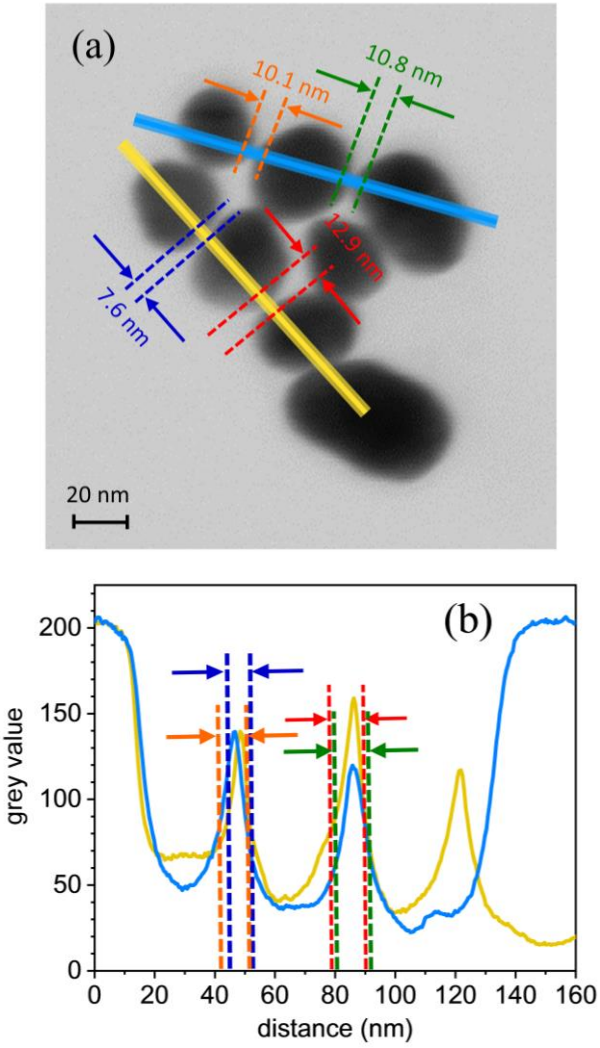

Fig. 4. (a) Analysis of the STEM images of a cluster made by functionalized AuNPs. In yellow and cyan the profiles along which the intensity plots shown in (b) are evaluated.

a mesh. Maxwell's equations were solved numerically in the time domain by evaluating the time evolution of the EM field in each sampled volume whose physical parameters were well-known. The time required to perform the simulation critically depended on the mesh settings, thus to ensure a good compromise between the reliability of the simulated absorbance spectra [29] and a reasonable simulation time, a spatial step of 0.5 nm was set for the mesh. We chose the so-called symmetric/anti-symmetric BCs for the geometries that exhibited one or more symmetry/anti-symmetry planes through the middle of the simulation region, whereas periodic BCs or Bloch BCs were adopted for the non-symmetric configurations. Symmetric BCs act as mirrors for the electric field and anti-mirrors for the magnetic field, while the opposite holds for anti-symmetric BCs. Thus, by taking advantage of possible symmetries/anti-symmetries of the workspace, it was possible to reduce the simulation volume (and time) by a factors of 2, 4 or 8 without worsening the accuracy of the result. In the absence of symmetry/anti-symmetry planes, periodic BCs were set to emulate as much as possible the behaviour of the EM field in the whole cuvette volume (1 mL). Since the Ab-AuNP aggregates were far apart in the solution, the EM field arisen from each aggregate did not affect the other. Thus, the workspace (i.e. the single Ab-AuNP aggregate and the surrounding water) represented the unit cell of the simulation in which the EM fields that occurred at one edge of the volume were re-injected at the other edge. Bloch BCs were adopted for non-symmetric geometries illuminated with a plane wave source to compensate the phase shift that arises when the EM field with a non-zero angle of incidence is re-injected at the opposite side. Perfect matched layer (PML) BCs were set on the volume boundaries corresponding to the position of the light source and of the photodetector for all the simulations to ensure the perfect absorption of the EM waves incident upon them [48]

A schematic representation of the simulation workspace is shown in the figure S7. The light source consisted of a plane wave source with a wavelength range from 400 nm to 700 nm, the embedding medium was water [49], the AuNPs were modelled as homogeneous gold spheres [50] and the Abs anchored to the gold surface were considered as a protein shell around the nanoparticle with a refraction index of 1.42

[51]. The Ab-AuNPs were arranged in the water volume according to the desired geometry. The transmission spectra were acquired by a photodetector located to the opposite side of the light source with a plot intervals of 1 nm.

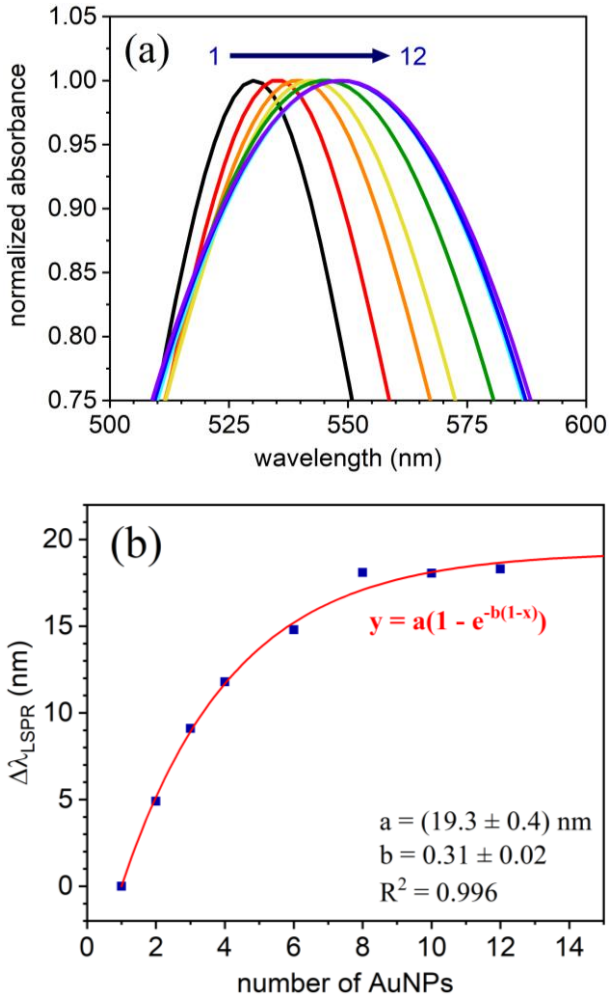

Fig. 5. (a) Gaussian fits of the simulated absorption peak for linear chains from 1 to 12 AuNPs. Each simulated spectrum $A(\lambda, \theta, N)$ was achieved by "FDTD Solutions" tool of the software Lumerical. (b) LSPR shift of the average absorption spectra as a function of the AuNP number along the chain.

In accordance with the diffusion-limited aggregation (DLA) model, it was reasonable to assume that AuNPs experienced a random walk (Brownian motion) and aggregated exhibiting a quasi-fractal artwork [52] (figure S5). Although a thoroughly analysis of such complex systems goes beyond the aims of this work, some of them (table S1) were investigated to elucidate the role of the linear dimension against the number of AuNPs. The simulated absorption spectra (figure S8) and the electric field distributions (table S2) showed that the optical response was essentially due to the linear branches contained in the structures

[53]. For instance, if we consider the electrical field distribution of the 2D asymmetrical geometry for 12 AuNPs (see table S2), the strongest coupling among the nanoparticles is achieved along the x direction and arises essentially from the two branches with 6 AuNPs. The LSPR wavelength for such a configuration (12 AuNPs, 2D asymmetric) is 552 nm that corresponds to the LSPR of 551 nm for a linear chain of 5 AuNPs aligned with the polarization direction (see figure S8).

Since the linear branches dominate the optical response of the clusters [54], to capture the essential physics behind the aggregation phenomenon, we simulated the plasmonic behaviour of the aggregates by considering them as linear chains of nanoparticles. We worked out the simulated absorption spectra $A(\theta, \lambda, N)$ and the electrical field distribution by varying the angle θ between the polarization direction of the light and the linear chain from 0° (longitudinal mode) to 90° (transversal mode), and the number N of AuNPs from 1 to 12. An example of such a calculation for a linear chain with 3 AuNPs is shown in figures S9a and S9b. While the maximum LSPR shift for a single chain took place at $\theta = 0°$ (electric field parallel to chain), the contributions from chains oriented at approximately $\theta = 90°$ (electric field transverse to chain) are vanishingly small (see figure S9a) resulting in a damped effect when the average over the whole distribution is worked out. In fact, when randomly oriented linear chains are considered, the dependence on the solid angle reduces to $\sin(\theta)$ in consideration of the cylindrical symmetry around the direction of the electric field; thus, we have

$$\bar{A}(\lambda, N) = \int_0^{\pi/2} A(\theta, \lambda, N) \sin(\theta)\, \mathrm{d}\theta \qquad (1)$$

The mean optical response $\bar{A}(\lambda, N)$ was worked out by summing up nine spectra at polarization angles from 0° to 90° with a step of 10°. The LSPR red-shift is clearly visible in figure 5a that reported the Gaussian fit of the absorption peak for linear chains from 1 to 12 AuNPs (see figure S10 for the mean simulated spectra). The behaviour of LSPR shift $\Delta\lambda_{LSPR}$ as a function of the number of AuNPs along the linear chain is shown in figure 5b and is well fitted by the equation

$$\Delta\lambda_{LSPR}(x) = a\left(1 - \mathrm{e}^{-b(x-1)}\right) \quad (2)$$

with $a = (19.3 \pm 0.4)$ nm and $b = 0.31 \pm 0.02$. The behaviour of the LSPR shift shown in figure 5b reproduces quite accurately the experimental data for relatively low LSPR shifts, that correspond to concentrations in the range 0-6 pg/mL and 20-10^5 pg/mL that led to clusters whose size did not exceed 5-6 AuNPs (see figures 3 and S5).

For linear chains with more AuNPs, the LSPR shift from equation (2) tends to saturate at approximately 19 nm, a value that is lower than 25 nm measured at 10 pg/mL (see figure 3). This discrepancy may well be explained by considering that the actual morphology of the aggregates was 2- and 3-dimensional. In fact, the damped effect experienced by averaging the linear chains on the solid angle is less significant when the structure to be rotate in the space has a complex 2- or 3-dimensional morphology, since at any angle it forms with the direction of the electric field, there are still significant contributions from linear branches included in the structure. Therefore, the shift behaviour described by equation (2) is an underestimation of the actual experimental shift around the *hook point*.

3.4. Dynamics of the aggregation

In order to provide a simplified approach to explain the AuNPs aggregation dynamics [30,55], we can suppose that the solution contains two species of Ab-AuNPs: E2-Ab-AuNPs (species A), namely the AuNPs whose Abs have bound the analytes, and the free Ab-AuNPs (species B) that are available to bind the analyte. The concentration of both species is linked by the relation $[\mathrm{A}] + [\mathrm{B}] = [\mathrm{AuNPs}]_0$, where the right-hand side represent the initial concentration of Ab-AuNP. At dynamic equilibrium, we have:

$$[\mathrm{A}] = \frac{[\mathrm{AuNPs}]_0 \cdot [\mathrm{E2}]}{K + [\mathrm{E2}]} \quad (3)$$

$$[\mathrm{B}] = [\mathrm{AuNPs}]_0 - [\mathrm{A}] = [\mathrm{AuNPs}]_0 \frac{K}{K + [\mathrm{E2}]} \quad (4)$$

where K is the equilibrium constant of the reaction $\mathrm{B} + \mathrm{E2} \leftrightarrow \mathrm{A}$. In this simple model, it is easy to realize that an excess of A or B shifts the equilibrium to the right or left of the *hook point*, respectively. The aggregation dynamics, and hence the cluster size, is a multiple-order complexation between A and B, which can be accounted for the following semi-empirical equation [56]

$$b(x-1) = \left(\frac{R[\mathrm{E2}]}{(K+[\mathrm{E2}])^2}\right)^n \tag{5}$$

where the factor R includes both the AuNP concentration and instrument response. The optical response of the colorimetric immunosensor as a function of the analyte concentration can be obtained by inserting equation (5) into equation (2). In doing this, we replaced the term a by an effective coefficient a_{eff} to take into account the actual LSPR shift occurring around the maximum; thus, we have

$$\Delta\lambda_{LSPR}([E2]) = a_{eff}\left(1 - \mathrm{e}^{-\left(\frac{R[\mathrm{E2}]}{(K+[\mathrm{E2}])^2}\right)^n}\right) \tag{6}$$

The data in figure 3 are well fitted by equation (6) with $a_{eff} = 25.4$ nm, $R = (43 \pm 3)$ pg mL^{-1}, $K = (10.4 \pm 0.7)$ pg mL^{-1} and $n = 19 \pm 6$, thereby confirming the effectiveness of the proposed approach to describe the complex aggregation dynamics occurring in this experiment. The coefficient a_{eff} was fixed to 25.4 nm, that corresponded to the maximum measured experimental shift.

While this model captures the cluster formation, it fails to reproduce the asymptotic behaviour of the AuNP aggregation occurring at higher E2 concentrations (black dash line in the figure 3). This is due to its inherent simplicity which does not include the complex diffusion process that took place in the whole interaction volume; in particular, even if the binding sites of Ab-AuNPs are locally fully saturated with E2 at high concentration - and hence no aggregation should arise among E2-Ab-AuNPs - these nanoparticles can form aggregates with Ab-AuNPs during their diffusion. This was proved by the STEM pictures since dimer and trimer contributions were clearly visible at 50 pg/mL of E2 (figure S5). To make this clear, we added the dashed curve in figure 3 that represents the "actual" asymptotic behaviour of the

immunosensor. Thus, while a detailed description of the aggregation dynamics should include a complex diffusion process, which goes beyond the scope of the present work, we point out that our biosensor is able to provide measurable signal even at very high E2 concentration, where usually the *hook effect* results in the false negative response.

3.5. Repeatability, stability, recovery and specificity assay

The repeatability of the immunosensor response was evaluated by comparing the LSPR shift of several measurements at E2 concentration of 10 pg/mL. The figures S11a and S11b showed a great reproducibility of the LSPR shift: Only two measurements out of ten fall outside the 67% confidence interval. The stability was studied by acquiring the absorption spectra of a single sample at E2 concentration of 10 pg/mL after different time intervals from the first measurement. The figure S11c confirmed the reliability and the long-term stability of the proposed colorimetric biosensor in terms of both functionalization effectiveness and analyte binding. The recovery was assessed for four E2 concentrations (4, 6, 12, 20 pg/mL) and the corresponding values are reported in table S3. The fluctuations from the nominal value of the measured E2 concentration are in the range of 10-25%, a value that is compatible with the experimental error bars (figure 3). The specificity of the immunosensor was proved by detection of the most competitive molecules of E2: progesterone, estrogens (E1 and E3) and testosterone. Figure 6 shows the reliability of the

immune response at low and high concentration of the interferences: While no detectable signal was observed for progesterone and testosterone, a very small response could be measured for E1 and E3 as a result of the partial lack of specificity of the Abs used for the functionalization. This does not prevent one from using the biosensor since any unlikely false positive due to E1 and E3 detection is anyway important as they are strongly involved in the estrogen metabolism [57].

4. Conclusions

The colorimetric immunosensor reported here is based on AuNPs functionalized with antibodies for the detection of a small molecule like 17β-estradiol. The high specificity, very low LOD (3 pg/mL) and affordable price are the main strengths of the proposed approach. The specificity is inherently ensured by the Ab functionalization whereas the plasmonic properties of AuNPs provide an accurate optical transduction of the biological signal. Moreover, the AuNP functionalization via PIT contributes to increase the biosensor sensitivity and long-term stability thanks to the covalent anchorage of the Abs on gold surface in upright orientation. The analyte detection arises from the change of the optical properties of the solution

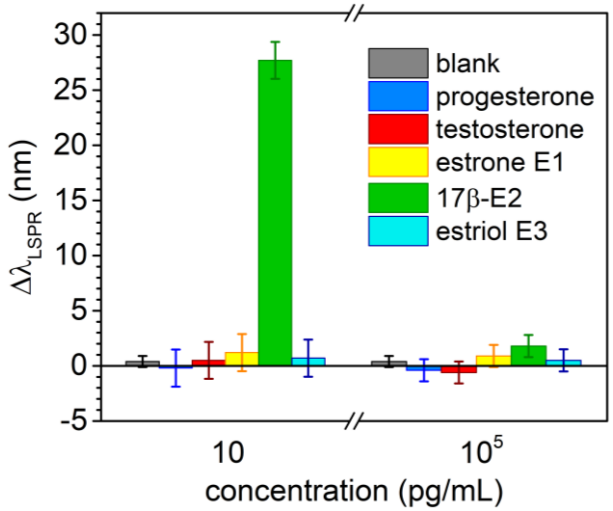

Fig. 6. Specificity assay. Shift of the absorption peak for different analytes at 10 pg/mL and 10^5 pg/mL.

due to the AuNP aggregation. Since the LSPR wavelength of isolated AuNPs as well as that of their aggregates falls in the visible region, the shift of the absorption peak following the analyte concentration entails a colour change visible by naked eyes. This allows a fast and qualitative test to establish the analyte

presence in the sample solution viable *in situ*. A quantitative measurement of the analyte concentration only requires an UV-vis spectrophotometer to assess carefully the wavelength of the absorption peak and hence to evaluate the LSPR shift.

Our colorimetric immunosensor is able to detect E2 in tap water down to 3 pg/mL within few hours after a 20 µL sample is added to cuvette containing 1 mL of Ab-AuNPs and represents a significant improvement in E2 low levels determination (without any preconcentration step) in terms of LOD, sample preparation, cost and analysis simplicity, thus challenging the usual expensive instrumental laboratory methods. Although in the current paper the mixing was performed by a vortex mixer to warrant high reproducibility, we observed that simple mechanical pipetting led to a detection time of few minutes, thus showing that the mixing procedure can be further optimized. Moreover, we demonstrated that in our procedure the *hook effect* does not lead to a vanishingly small signal, but to a semi-quantitative response that can be used as an alert signal. Nevertheless, should a quantitative response be required, it is possible to resort to serial dilutions of the sample, a procedure that is customary in immunoassays [58]; for instance, in our case, four dilutions such as 1:2, 1:5, 1:10 and 1:100 would be suitable to cover the quantification at higher concentration up to 1 ng/mL (see table S4). The reduction of the time required for the mixing process combined with the availability of portable and handheld VIS spectrophotometers will make the proposed biosensor very promising for routinely *in situ* E2 monitoring of river waters.

The range of the investigated E2 concentration is of interest in several diagnostic and environmental contexts suggesting the possibility to extend our colorimetric biosensors to other matrices (e.g. urine and wastewater) although some pretreatment step such as desalination, purification or pH modification might be necessary. Furthermore, the scheme described here can be adopted for different analytes (e.g. ochratoxin A and aflatoxin B1) by simply changing the antibody.

CRediT authorship contribution statement

A. M.[a,b] and N. S.[c] contributed equally to the work.

Acknowledgements

This work was supported by the European Cooperation in Science and Technology Action CA16215 European network for the promotion of portable, affordable and simple analytical platforms.

References

[1] P. Habib, D. Dreymueller, B. Rösing, H. Botung, A. Slowik, A. Zendedel, S. Habib, S. Hoffmann, C. Beyer, Estrogen serum concentration affects blood immune cell composition and polarization in human females under controlled ovarian stimulation, J. Steroid Biochem. Mol. Biol. 178 (2018) 340–347. https://doi.org/10.1016/j.jsbmb.2018.02.005.

[2] J.-M. Tian, B. Ran, C.-L. Zhang, D.-M. Yan, X.-H. LI, J.-M. Tian, B. Ran, C.-L. Zhang, D.-M. Yan, X.-H. LI, Estrogen and progesterone promote breast cancer cell proliferation by inducing cyclin G1 expression, Brazilian J. Med. Biol. Res. 51 (2018) 1–7. https://doi.org/10.1590/1414-431x20175612.

[3] J.P. Sumpter, Endocrine Disrupters in the Aquatic Environment: An Overview, Acta Hydrochim. Hydrobiol. 33 (2005) 9–16. https://doi.org/10.1002/aheh.200400555.

[4] T.F.T. Omar, A. Ahmad, A.Z. Aris, F.M. Yusoff, Endocrine disrupting compounds (EDCs) in environmental matrices: Review of analytical strategies for pharmaceuticals, estrogenic hormones, and alkylphenol compounds, TrAC Trends Anal. Chem. 85 (2016) 241–259. https://doi.org/10.1016/j.trac.2016.08.004.

[5] A.S. Kolok, J.M. Ali, E.G. Rogan, S.L. Bartelt-Hunt, The fate of synthetic and endogenous hormones used in the us beef and dairy industries and the potential for human exposure, Curr. Environ. Heal. Reports. 5 (2018) 225–232. https://doi.org/10.1007/s40572-018-0197-9.

[6] R. Xuan, A.A. Blassengale, Q. Wang, Degradation of estrogenic hormones in a silt loam soil, J. Agric. Food Chem. 56 (2008) 9152–9158. https://doi.org/10.1021/jf8016942.

[7] S. Arnon, O. Dahan, S. Elhanany, K. Cohen, I. Pankratov, A. Gross, Z. Ronen, S. Baram, L.S. Shore, Transport of testosterone and estrogen from dairy-farm waste lagoons to groundwater, Environ. Sci. Technol. 42 (2008) 5521–5526. https://doi.org/10.1021/es800784m.

[8] F. Brion, C.. Tyler, X. Palazzi, B. Laillet, J.. Porcher, J. Garric, P. Flammarion, Impacts of 17β-estradiol, including environmentally relevant concentrations, on reproduction after exposure during embryo-larval-, juvenile- and adult-life stages in zebrafish (Danio rerio), Aquat. Toxicol. 68 (2004) 193–217. https://doi.org/10.1016/j.aquatox.2004.01.022.

[9] S. González, R. López-Roldán, J.-L. Cortina, Presence and biological effects of emerging contaminants in Llobregat River basin: A review, Environ. Pollut. 161 (2012) 83–92. https://doi.org/10.1016/j.envpol.2011.10.002.

[10] C. Liscio, E. Magi, M. Di Carro, M.J.F. Suter, E.L.M. Vermeirssen, Combining passive samplers and biomonitors to evaluate endocrine disrupting compounds in a wastewater treatment plant by LC/MS/MS and bioassay analyses, Environ. Pollut. 157 (2009) 2716–2721. https://doi.org/10.1016/j.envpol.2009.04.034.

[11] M. Dou, K. Zhu, Z. Fan, Y. Zhang, X. Chen, X. Zhou, X. Ding, L. Li, Z. Gu, M. Guo, M. Yan, X. Deng, P. Shen, S. Wang, Reproductive Hormones and Their Receptors May Affect Lung Cancer, Cell. Physiol. Biochem. 44 (2017) 1425–1434. https://doi.org/10.1159/000485538.

[12] P.P. Liu, X. Liu, X.H. Huo, Y. Tang, J. Xu, H. Ju, TiO2-BiVO4 Heterostructure to Enhance Photoelectrochemical Efficiency for Sensitive Aptasensing, ACS Appl. Mater. Interfaces. 9 (2017) 27185–27192. https://doi.org/10.1021/acsami.7b07047.

[13] M.A. Nameghi, N.M. Danesh, M. Ramezani, M. Alibolandi, K. Abnous, S.M. Taghdisi, An ultrasensitive electrochemical sensor for 17β-estradiol using split aptamers, Anal. Chim. Acta. 1065 (2019) 107–112. https://doi.org/10.1016/j.aca.2019.02.062.

[14] A.A. Lahcen, A.A. Baleg, P. Baker, E. Iwuoha, A. Amine, Synthesis and electrochemical characterization of

nanostructured magnetic molecularly imprinted polymers for 17-β-Estradiol determination, Sensors Actuators, B Chem. 241 (2017) 698–705. https://doi.org/10.1016/j.snb.2016.10.132.

[15] X. Ni, B. Xia, L. Wang, J. Ye, G. Du, H. Feng, X. Zhou, T. Zhang, W. Wang, Fluorescent aptasensor for 17β-estradiol determination based on gold nanoparticles quenching the fluorescence of Rhodamine B, Anal. Biochem. 523 (2017) 17–23. https://doi.org/10.1016/j.ab.2017.01.021.

[16] G. Zhang, T. Li, J. Zhang, A. Chen, A simple FRET-based turn-on fluorescent aptasensor for 17B-estradiol determination in environmental water, urine and milk samples, Sensors Actuators, B Chem. 273 (2018) 1648–1653. https://doi.org/10.1016/j.snb.2018.07.066.

[17] J. Liu, W. Bai, S. Niu, C. Zhu, S. Yang, A. Chen, Highly sensitive colorimetric detection of 17β-estradiol using split DNA aptamers immobilized on unmodified gold nanoparticles, Sci. Rep. 4 (2014). https://doi.org/10.1038/srep07571.

[18] J.N. Siew, X. Su, J.S. Thomsen, Surface plasmon resonance study of cooperative interactions of estrogen receptor α and transcriptional factor Sp1 with composite DNA elements, Anal. Chem. 81 (2009) 3344–3349. https://doi.org/10.1021/ac802543x.

[19] S. Kumbhat, R. Gehlot, K. Sharma, U. Singh, V. Joshi, Surface plasmon resonance based indirect immunoassay for detection of 17β-estradiol, J. Pharm. Biomed. Anal. 163 (2019) 211–216. https://doi.org/10.1016/j.jpba.2018.10.015.

[20] X. Yao, Z. Wang, L. Dou, B. Zhao, Y. He, J. Wang, J. Sun, T. Li, D. Zhang, An innovative immunochromatography assay for highly sensitive detection of 17B-estradiol based on an indirect probe strategy, Sensors Actuators, B Chem. (2019) 48–55. https://doi.org/10.1016/j.snb.2019.03.078.

[21] S.U. Akki, C.J. Werth, Critical Review: DNA Aptasensors, Are They Ready for Monitoring Organic Pollutants in Natural and Treated Water Sources?, Environ. Sci. Technol. 52 (2018) 8989–9007. https://doi.org/10.1021/acs.est.8b00558.

[22] S.A. Maier, Plasmonics: Fundamentals and Applications, Springer US, New York, NY, NY, 2007. https://doi.org/10.1007/0-387-37825-1.

[23] P. Uebel, S.T. Bauerschmidt, M.A. Schmidt, P. St.j. Russell, A gold-nanotip optical fiber for plasmon-enhanced near-field detection, Appl. Phys. Lett. 103 (2013). https://doi.org/10.1063/1.4813115.

[24] S.K. Patel, C. Argyropoulos, Plasmonic nanoantennas: enhancing light-matter interactions at the nanoscale, EPJ Appl. Metamaterials. 2 (2015) 4. https://doi.org/10.1051/epjam/2015006.

[25] A. V. Kabashin, P. Evans, S. Pastkovsky, W. Hendren, G.A. Wurtz, R. Atkinson, R. Pollard, V.A. Podolskiy, A. V. Zayats, Plasmonic nanorod metamaterials for biosensing, Nat. Mater. 8 (2009) 867–871. https://doi.org/10.1038/nmat2546.

[26] S.H. Kim, S.M. Sharker, H. Lee, I. In, K.D. Lee, S.Y. Park, Photothermal conversion upon near-infrared irradiation of fluorescent carbon nanoparticles formed from carbonized polydopamine, RSC Adv. 6 (2016) 61482–61491. https://doi.org/10.1039/c6ra08196g.

[27] O.A. Alsager, S. Kumar, B. Zhu, J. Travas-Sejdic, K.P. McNatty, J.M. Hodgkiss, Ultrasensitive colorimetric detection of 17-estradiol: The effect of shortening dna aptamer sequences, Anal. Chem. 87 (2015) 4201–4209. https://doi.org/10.1021/acs.analchem.5b00335.

[28] R. Wang, H. Chon, S. Lee, Z. Cheng, S.H. Hong, Y.H. Yoon, J. Choo, Highly Sensitive Detection of Hormone Estradiol E2 Using Surface-Enhanced Raman Scattering Based Immunoassays for the Clinical Diagnosis of Precocious Puberty, ACS Appl. Mater. Interfaces. 8 (2016) 10665–10672. https://doi.org/10.1021/acsami.5b10996.

[29] P.N. Njoki, I.-I.S. Lim, D. Mott, H.-Y. Park, B. Khan, S. Mishra, R. Sujakumar, J. Luo, C.-J. Zhong, Size Correlation of Optical and Spectroscopic Properties for Gold Nanoparticles, J. Phys. Chem. C. 111 (2007) 14664–14669. https://doi.org/10.1021/jp074902z.

[30] S.K. Ghosh, T. Pal, Interparticle Coupling Effect on the Surface Plasmon Resonance of Gold Nanoparticles: From Theory to Applications, Chem. Rev. 107 (2007) 4797–4862. https://doi.org/10.1021/cr0680282.

[31] R. Shukla, V. Bansal, M. Chaudhary, A. Basu, R.R. Bhonde, M. Sastry, Biocompatibility of gold nanoparticles and their endocytotic fate inside the cellular compartment: A microscopic overview, Langmuir. 21 (2005) 10644–10654. https://doi.org/10.1021/la0513712.

[32] X. Zhang, Gold Nanoparticles: Recent Advances in the Biomedical Applications, Cell Biochem. Biophys. 72 (2015) 771–775. https://doi.org/10.1007/s12013-015-0529-4.

[33] A. Chaudhary, S. Khan, A. Gupta, C.K. Nandi, Effect of surface chemistry and morphology of gold nanoparticle on

the structure and activity of common blood proteins†, New J. Chem. 40 (2016) 4879–4883. https://doi.org/10.1039/C5NJ03720D.

[34] P. Tiwari, K. Vig, V. Dennis, S. Singh, Functionalized Gold Nanoparticles and Their Biomedical Applications, Nanomaterials. 1 (2011) 31–63. https://doi.org/10.3390/nano1010031.

[35] B. Della Ventura, L. Schiavo, C. Altucci, R. Esposito, R. Velotta, Light assisted antibody immobilization for biosensing, Biomed. Opt. Express. 2 (2011) 3223–3231. https://doi.org/10.1364/BOE.2.003223.

[36] R. Funari, B. Della Ventura, C. Altucci, A. Offenhäusser, D. Mayer, R. Velotta, Single Molecule Characterization of UV-Activated Antibodies on Gold by Atomic Force Microscopy, Langmuir. 32 (2016) 8084–8091. https://doi.org/10.1021/acs.langmuir.6b02218.

[37] B. Della Ventura, M. Banchelli, R. Funari, A. Illiano, M. De Angelis, P. Taroni, A. Amoresano, P. Matteini, R. Velotta, Biosensor surface functionalization by a simple photochemical immobilization of antibodies: experimental characterization by mass spectrometry and surface enhanced Raman spectroscopy, Analyst. 144 (2019) 6871–6880. https://doi.org/10.1039/C9AN00443B.

[38] R. Funari, B. Della Ventura, L. Schiavo, R. Esposito, C. Altucci, R. Velotta, Detection of parathion pesticide by quartz crystal microbalance functionalized with UV-activated antibodies., Anal. Chem. 85 (2013) 6392–7. https://doi.org/10.1021/ac400852c.

[39] R. Funari, B. Della Ventura, R. Carrieri, L. Morra, E. Lahoz, F. Gesuele, C. Altucci, R. Velotta, Detection of parathion and patulin by quartz-crystal microbalance functionalized by the photonics immobilization technique, Biosens. Bioelectron. 67 (2015) 224–229. https://doi.org/10.1016/j.bios.2014.08.020.

[40] B. Della Ventura, N. Sakač, R. Funari, R. Velotta, Flexible immunosensor for the detection of salivary α-amylase in body fluids, Talanta. 174 (2017) 52–58. https://doi.org/10.1016/j.talanta.2017.05.075.

[41] B. Della Ventura, M. Iannaccone, R. Funari, M. Pica Ciamarra, C. Altucci, R. Capparelli, S. Roperto, R. Velotta, Effective antibodies immobilization and functionalized nanoparticles in a quartz-crystal microbalance-based immunosensor for the detection of parathion, PLoS One. 12 (2017) e0171754. https://doi.org/10.1371/journal.pone.0171754.

[42] M.J. Pollitt, G. Buckton, R. Piper, S. Brocchini, Measuring antibody coatings on gold nanoparticles by optical spectroscopy, RSC Adv. 5 (2015) 24521–24527. https://doi.org/10.1039/C4RA15661G.

[43] W. Haiss, N.T.K. Thanh, J. Aveyard, D.G. Fernig, Determination of size and concentration of gold nanoparticles from UV-Vis spectra, Anal. Chem. 79 (2007) 4215–4221. https://doi.org/10.1021/ac0702084.

[44] N.A. Byzova, I. V. Safenkova, E.S. Slutskaya, A. V. Zherdev, B.B. Dzantiev, Less is More: A Comparison of Antibody-Gold Nanoparticle Conjugates of Different Ratios, Bioconjug. Chem. 28 (2017) 2737–2746. https://doi.org/10.1021/acs.bioconjchem.7b00489.

[45] T. Kim, C.H. Lee, S.W. Joo, K. Lee, Kinetics of gold nanoparticle aggregation: Experiments and modeling, J. Colloid Interface Sci. 318 (2008) 238–243. https://doi.org/10.1016/j.jcis.2007.10.029.

[46] J. Miller, Interference in immunoassays : avoiding erroneous results, Clin. Lab. Int. 28 (2004) 14–17.

[47] P.K. Jain, W. Huang, M.A. El-Sayed, On the universal scaling behavior of the distance decay of plasmon coupling in metal nanoparticle pairs: A plasmon ruler equation, Nano Lett. 7 (2007) 2080–2088. https://doi.org/10.1021/nl071008a.

[48] J.-P. Bérenger, Perfectly Matched Layer (PML) for Computational Electromagnetics, Synth. Lect. Comput. Electromagn. 2 (2007) 1–117. https://doi.org/10.2200/s00030ed1v01y200605cem008.

[49] Edward D. Palik, Refractive Index, in: Handb. Opt. Constants Solids, Elsevier, 1997: pp. 5–114. https://doi.org/10.1016/B978-012544415-6.50149-7.

[50] P.B. Johnson, R.W. Christy, Optical constants of the noble metals, Phys. Rev. B. 6 (1972) 4370–4379. https://doi.org/10.1103/PhysRevB.6.4370.

[51] N.C. Bell, C. Minelli, A.G. Shard, Quantitation of IgG protein adsorption to gold nanoparticles using particle size measurement, Anal. Methods. 5 (2013) 4591. https://doi.org/10.1039/c3ay40771c.

[52] T.A. Witten, L.M. Sander, Diffusion-limited aggregation, Phys. Rev. B. 27 (1983) 5686–5697. https://doi.org/10.1103/PhysRevB.27.5686.

[53] D. Zámbó, A. Deák, Optical simulations of self-assembly relevant gold aggregates: A comparative study, Period.

Polytech. Chem. Eng. 60 (2016) 244–251. https://doi.org/10.3311/PPch.9101.

[54] R.W. Taylor, R. Esteban, S. Mahajan, R. Coulston, O.A. Scherman, J. Aizpurua, J.J. Baumberg, Simple composite dipole model for the optical modes of strongly-coupled plasmonic nanoparticle aggregates, J. Phys. Chem. C. 116 (2012) 25044–25051. https://doi.org/10.1021/jp308986c.

[55] N.M. Kovalchuk, V.M. Starov, Aggregation in colloidal suspensions: Effect of colloidal forces and hydrodynamic interactions, Adv. Colloid Interface Sci. 179–182 (2012) 99–106. https://doi.org/10.1016/j.cis.2011.05.009.

[56] M. Iarossi, C. Schiattarella, I. Rea, L. De Stefano, R. Fittipaldi, A. Vecchione, R. Velotta, B. Della Ventura, Colorimetric Immunosensor by Aggregation of Photochemically Functionalized Gold Nanoparticles, ACS Omega. 3 (2018) 3805–3812. https://doi.org/10.1021/acsomega.8b00265.

[57] H. Kuhl, Pharmacology of estrogens and progestogens: Influence of different routes of administration, Climacteric. 8 (2005) 3–63. https://doi.org/10.1080/13697130500148875.

[58] A. Dasgupta, A. Wahed, Laboratory Statistics and Quality Control, in: Clin. Chem. Immunol. Lab. Qual. Control, 2014: pp. 47–66. https://doi.org/10.1016/B978-0-12-407821-5.00004-8.